POLITECNICO DI TORINO
Repository ISTITUZIONALE

High-Contrast Gratings Performance Issues in Tunable VCSELs

(Article begins on next page)

24 April 2024

High-Contrast Gratings
Performance Issues in Tunable VCSELs

Alberto Tibaldi, Pierluigi Debernardi, and Renato Orta, *Senior Member, IEEE*

Abstract—Tunable vertical-cavity surface-emitting lasers (VCSELs) are becoming key components in several sensing applications, where single mode, single polarization light is required. In such devices, high-contrast gratings are very promising mirrors, because of their high reflectivity, strong polarization discrimination, and low volume occupation. However, their introduction might lead to unexpected increases of the threshold gain, destroying the tuning performance. In this paper these phenomena are investigated and explained in detail. Although VCSEL modes are computed by means of the full 3-D vectorial code VELM, a Gaussian beam model is used to obtain deeper insight into the HCG reflectivity mechanism in presence of a finite beam.

Index Terms—Tunable VCSELs, periodic structures, dielectric structures, high-contrast gratings.

Fig. 1. Schematic of the mid-IR tunable VCSEL [10], where the top mirror has been replaced by an HCG.

I. Introduction

VERTICAL-cavity surface-emitting lasers (VCSELs) are among the most interesting semiconductor laser diodes and have become market leaders since several years [1]. Tunable VCSELs, *i.e.* lasers with controllable emission wavelength, have been successfully demonstrated, first in GaAs-based devices [2], and later in InP-based structures [3], [4]. However, the development of these components is still at an early stage, and no tuning VCSEL is commercially available yet. Such devices are very sought after, because of the many possible applications: wavelength-division multiplexing (WDM), reconfigurable last-mile fiber communication systems, and especially the vast field of sensing. All these applications require single mode and stable polarization, making high-contrast gratings (HCGs) an ideal choice as integrated mirrors [5]-[9].

While the $800 - 2500$ nm range is already covered by GaAs and InP semiconductors, the mid-infrared (mid-IR) $3000 - 4500$ nm window is nearly unexplored. Therefore, this paper is focused on devices operating in this band, even if most of the results and conclusions are general. Mid-IR lasers would be very useful for the realization of state-of-the-art spectrometry equipments, because the absorption lines of many gases and polluting elements lay within this band. A possible solution to cover the 3000-4500 nm spectrum is to employ lead chalcogenite semiconductors. Tunable VCSELs based on this semiconductor system have been successfully demonstrated by using a distributed Bragg reflector (DBR) as top movable mirror [10]. In view of stabilizing the polarization features of such devices, in this paper we investigate the performance modifications (tuning features and threshold gain G_{th}) caused by replacing the DBR by an HCG.

HCG plane-wave reflectivity spectra can be obtained by means of full-wave electromagnetic simulators, *e.g.,* the rigorous-coupled wave analysis (RCWA) [11], [12]. Other approaches have been proposed: the spectral element method (SEM), which allows a much better grating mode approximation [13]; the mortar-element method, which is an extension of the SEM to complex geometries [14], [15]. In addition to these works, a mode-matching technique (MMT) based on the analytic expressions of the grating modes has been developed [16]; this is used to establish design guidelines for the normal incidence case.

According to the standard procedure, the HCG design has been performed starting from its normal-incidence plane wave reflectivity; the corresponding tuning performance and threshold gain can be estimated with a transfer matrix method where the HCG is simulated by one of the previous approaches [17]. These 1-D results usually provide a good estimate of the tuning features compared to the results of the full 3-D vectorial model VELM [18]-[19]. However, during this project, huge deviations between these two frameworks (1-D and 3-D) have been observed. In fact, during the tuning, the threshold gain might increase enormously compared to the 1-D result, leading to values higher than the ones provided by the active material. This paper is concerned with a deep investigation of this phenomenon, which is related to beam finiteness. To keep things as simple as possible in the HCG reflectivity analysis, a Gaussian beam excitation model has been exploited [17], [19]. This allows to account for the source finiteness, without

A. Tibaldi and P. Debernardi are with the Consiglio Nazionale delle Ricerche (CNR), Istituto di Elettronica e di Ingegneria dell'Informazione e delle Telecomunicazioni (IEIIT), 10129 Turin, Italy, e-mail: alberto.tibaldi@ieiit.cnr.it.

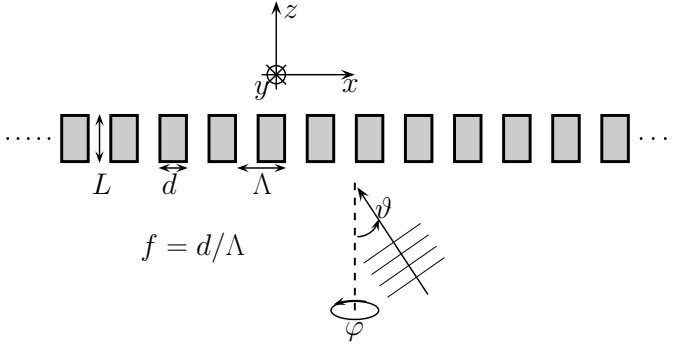R. Orta is with the Department of Electronics and Telecommunications, Politecnico di Torino, Torino, 10129 Italy.

Fig. 2. Sketch of the periodic structure composed of dielectric bars (refractive index n) in air, excited by a plane wave with polar and azimuth angles ϑ and φ.

studying the complicated 3-D structure. From these analyses it appears that the normal-incidence results are not always reliable, since the HCG angular dependence may deteriorate the grating reflection features, as already pointed out in [20], as an outcome of FDTD simulations.

In this work the reflectivity degradation mechanism is investigated through extensive theoretical analyses and its physical reason disclosed. In Section II a comparison of the 1-D and 3-D tuning features is presented. In Section III, the Gaussian beam analysis method is described and applied to the HCG used in Section II. In Section IV, the physical mechanism that deteriorates the reflectivity is explained in terms of Wood's anomalies [21].

TABLE I
HCG DESIGN PARAMETERS

Parameter	Design 1	Design 2
Λ	1425 nm	1350 nm
L	865 nm	920 nm
f	75%	61 %

II. MID-IR TUNABLE VCSEL DESIGN AND ANALYSIS

Figure 1 shows the investigated device, which is based on the structure described in [10]. The VCSEL has a de-

Fig. 4. VCSEL tuning features: emission wavelength (top) and threshold gain per quantum well (bottom) versus air-gap. Results are obtained by analyzing the device with a 1-D VCSEL simulator (light green curves) and with the full 3-D vectorial model VELM (solid blue curves).

sign wavelength of $3.45\,\mu$m. The bottom DBR consists of quarter-wavelength EuTe/Pb$_x$Eu$_{1-x}$Te pairs grown on Si ($n = 2.4/5.31$). The Pb$_y$Sr$_{1-y}$Se 1-λ cavity contains the PbSe quantum wells (QWs), which are positioned in correspondence of the optical standing wave peaks. Additional details can be found in [10]. The external top mirror is composed of Si bars in air [2], [20], as sketched in Fig. 2. This array is periodic along x with period Λ and uniform along y. Each bar has refractive index n, thickness L (along z) and filling factor f, defined as the ratio of its width d (along x) to Λ.

The air-gap varies around $10\,\mu$m to guarantee a wide free spectral range. The $1.55\,\mu$m pump laser is arranged on axis above the HCG mirror, which is designed so that its transmissivity is maximized at that wavelength. The mid-IR
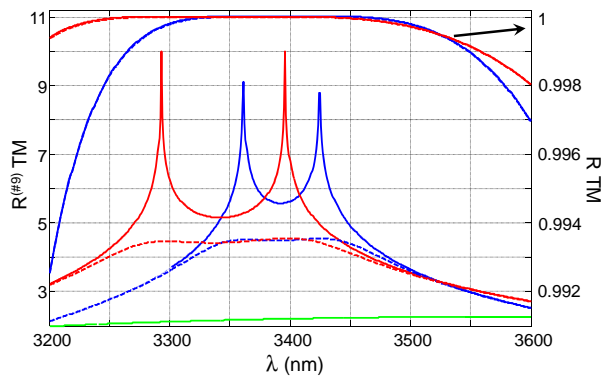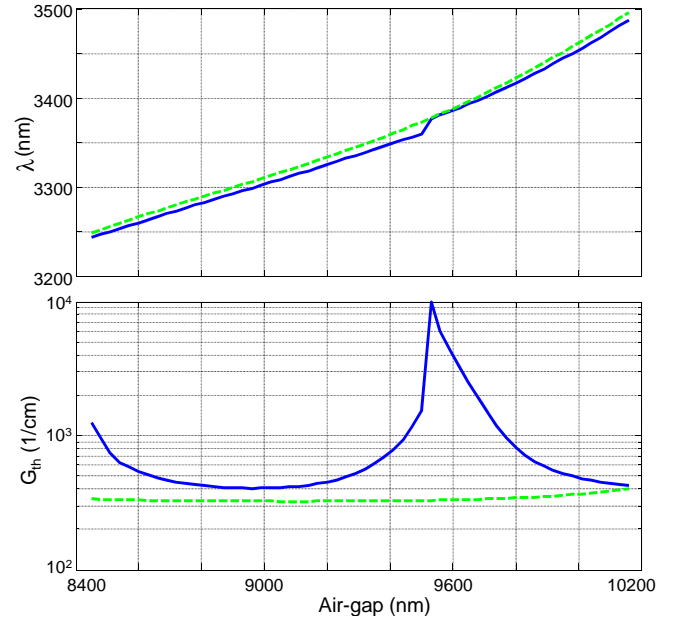

Fig. 3. Reflectivity spectra of Designs 1 (red), 2 (blue), and DBR (green) for normal-incidence plane-wave. Left: logarithmic scale; right: linear scale. Solid and dashed curves refer to the lossless and lossy cases; their difference can be observed only with the logarithmic scale.
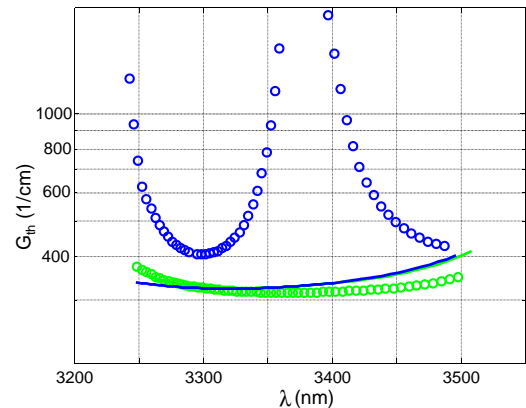

Fig. 5. Threshold gain versus emission wavelength. Blue and light green refer to Design 1 and 2. Solid curves and circles are obtained with the 1-D and 3-D simulators, respectively.
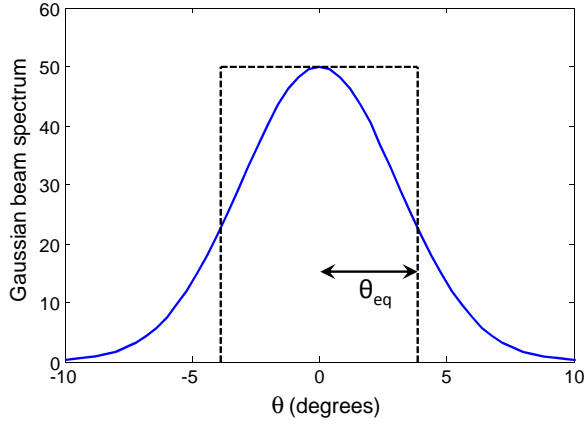
Fig. 6. The solid curve is the squared amplitude of the spectral components of the $w = 10\,\mu$m Gaussian beam, which approximates the actual VCSEL mode profile. The dashed rectangle, used to define the equivalent angular spectral width, has the same area as the Gaussian. In this example, $\vartheta_{\mathrm{eq}} = 3.86°$, at $\lambda = 3373$ nm (see Fig. 7).

laser beam escapes through the bottom Si-substrate, which must therefore have a much lower reflectivity than the HCG (around 0.995). After a preliminary study, two possible sets of parameters, reported in Table I, have been selected for the HCG of this tunable VCSEL.

The reflectivity spectra $R^{(\#9)}$ of the two designs at normal incidence are shown in Fig. 3 for the TM polarization in terms of "number of nines", *i.e.,*

$$R^{(\#9)} = -\log_{10}(1 - R),$$

where R is the power reflectivity. The logarithmic representation should be preferred to the linear one, since only the latter allows to appreciate variations in the $0.99 - 0.9999$ interval. This can be observed in Fig. 3, where the results are given in the two types of scale. This figure provides also the lower DBR reflectivity, which allows to get at a glance the wavelength range where the minimum top to bottom reflectivity ratio guarantees the radiation of most of the light at the output side (bottom, in this case).

It is observed that in the $3300 - 3500$ nm range the reflectivity levels stay in the required ratios. The performance of the two HCG designs, from now on called Design 1 and 2, are provided with reference to two situations: ideal lossless ($n_{\mathrm{Si}} = 3.6$) and slightly lossy Si ($n_{\mathrm{Si}} = 3.6 - \mathrm{j}10^{-5}$, 0.35 cm^{-1} absorption), which might account for intrinsic optical losses or small scattering due to bar-roughness inherent to HCG processing. The lossless reflectivity shows the usual two peaks that are exploited to achieve a wider high reflection band [16]; such peaks attain the exact value of 1, which cannot be observed in Fig. 3 for lack of sampling points. Figure 3 emphasizes that, when losses are accounted for, it is not reasonable to pursue more than 5 nines. From now on, these small losses will be included in the simulations.

The two HCGs have been preliminarily tested with a 1-D simulation of the complete VCSEL [17], which confirmed good tuning performance (> 200 nm around 3.4 μm, G_{th}

within $300 - 400$ cm^{-1}). Usually, 1-D simulations provide useful information about tuning range and threshold in tunable VCSELs [3], [17]. However, 3-D simulations are necessary to assess the transverse mode properties, which are particularly critical when strictly (transverse and polarization) single mode operations is required. In the 3-D case a circular mesa of $30\,\mu$m diameter forms the cavity (see Fig. 1, red part), with a corresponding active size. The pump beam width is assumed to be slightly larger than the mesa, to guarantee an active size of 30 μm. These structures have been simulated for various air-gaps by means of VELM, our in-house fully vectorial VCSEL code [19], and the results are reported in Fig. 4. Here, the VCSEL emission wavelengths and the corresponding threshold gains are computed by 1-D and 3-D models. A huge difference between the two results can be observed, with particular reference to the threshold gain. In fact, in the $3.35 - 3.4\,\mu$m range, lasing action can not be achieved because G_{th} reaches values 30 times higher than in the 1-D computation. Figure 5 reports a comparison between the 1-D and 3-D simulations for the two designs in the $(\lambda, G_{\mathrm{th}})$ plane; this is a synthetic representation of the tuning laser performance [22]. Here, it appears that the aforementioned 1-D – 3-D difference arises only for Design 1, whereas for Design 2 the 1-D and 3-D simulations are compatible. Therefore, Design 1 poses a serious issue on the HCG performance, which will be the main topic of the paper.

III. GAUSSIAN BEAM MODEL AND NUMERICAL RESULTS

From now on, the Design 1 will be used as a case study, for which a Gaussian beam excitation will be employed. The Gaussian beam, propagating along z, is impinging from below on the grating interface (see Fig. 2), with its electric field parallel to x (TM):

$$\mathbf{E}^{(\mathrm{inc})}(x,y) = H_m\left(\frac{\sqrt{2}}{w}x\right) H_n\left(\frac{\sqrt{2}}{w}y\right) \mathrm{e}^{-\frac{x^2+y^2}{w^2}}\hat{\mathbf{x}},$$

where $H_m(x)$ is the m-th degree Hermite polynomial, and w is the beam waist; this work focuses on the fundamental Gaussian beam, *i.e., $m = n = 0$.*

The following spectral representation is introduced:

$$\mathbf{E}^{(\mathrm{inc})}(x,y) = \frac{1}{(2\pi)^2}\int_{-\infty}^{+\infty}\int_{-\frac{\pi}{\Lambda}}^{+\frac{\pi}{\Lambda}} V_{\xi\eta}\mathbf{e}_{\xi\eta}(x,y)\,\mathrm{d}\xi\,\mathrm{d}\eta. \quad (1)$$

This corresponds to an expansion of the Gaussian beam in terms of Floquet modes, where each (ξ, η) defines a plane wave representing the 0 order of the reciprocal lattice (see (2)). The real numbers ξ and η are the x and y components of its incident wavevector; $\mathbf{e}_{\xi\eta}(x,y)$ and $V_{\xi\eta}$ are the eigenfunctions and the transform coefficients. The integrand of (1) is decomposed into TM and TE contributions:

$$V_{\xi\eta}^{(\mathrm{inc})}\mathbf{e}_{\xi\eta}(x,y) = \underbrace{V_{\xi\eta}^{(\mathrm{inc})'}\mathbf{e}_{\xi\eta}'(x,y)}_{\mathrm{TM}} + \underbrace{V_{\xi\eta}^{(\mathrm{inc})''}\mathbf{e}_{\xi\eta}''(x,y)}_{\mathrm{TE}}.$$
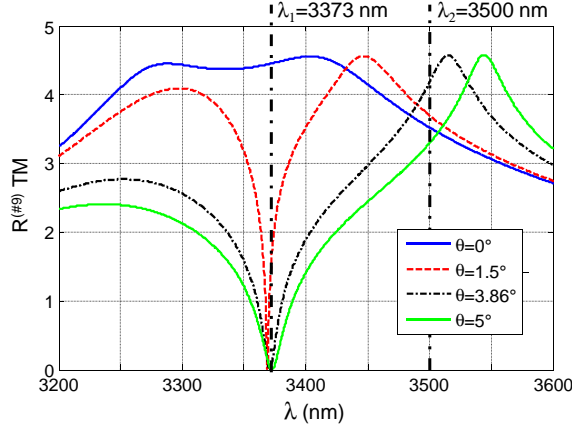
Here, given

Fig. 7. TM plane wave power reflectivity for Design 1. The curves refer to different angles ϑ, for $\varphi = 0°$. Definition of λ_1 and λ_2, used as case studies in the following figures.
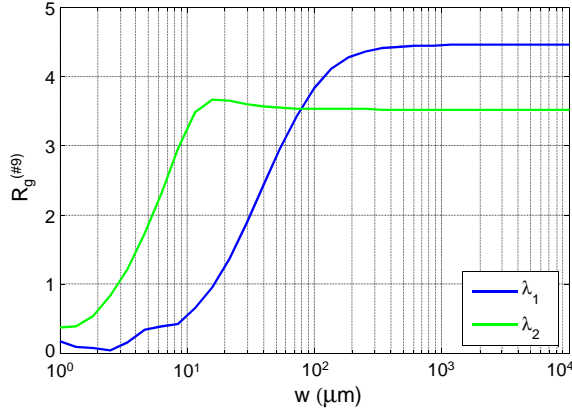

Fig. 8. HCG Gaussian beam reflectivity versus beam waist w; $n = 3.6 - j10^{-5}$

$$e_{\xi\eta}(x,y) = e^{-j\xi x}e^{-j\eta y}, \qquad (2)$$

and

$$\sigma = \sqrt{\xi^2 + \eta^2},$$

$$\mathbf{e}'_{\xi\eta}(x,y) = -\hat{\mathbf{x}}\frac{\xi}{\sigma}e_{\xi\eta}(x,y) - \hat{\mathbf{y}}\frac{\eta}{\sigma}e_{\xi\eta}(x,y)$$

$$\mathbf{e}''_{\xi\eta}(x,y) = -\hat{\mathbf{x}}\frac{\eta}{\sigma}e_{\xi\eta}(x,y) + \hat{\mathbf{y}}\frac{\xi}{\sigma}e_{\xi\eta}(x,y),$$

the Gaussian beam expansion coefficients are essentially the Fourier transform of $\mathbf{E}^{(\text{inc})}$.

Figure 6 reports the power spectral components of the $w = 10$ μm Gaussian beam as a function of the incidence angle ϑ; this choice provides a good fit with the actual field distribution incident on the HCG obtained from the full 3-D VCSEL simulator. The angle ϑ is defined as

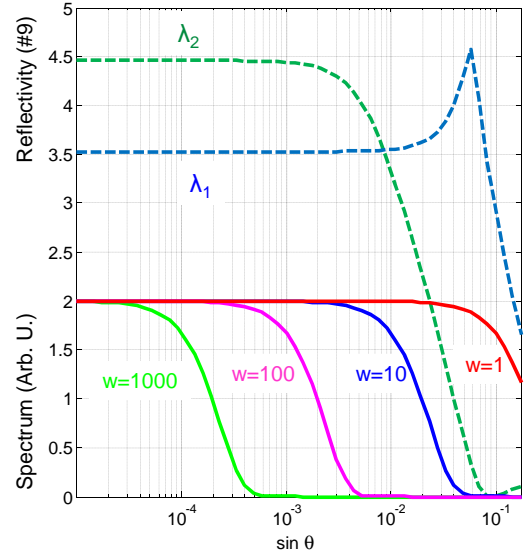$$\vartheta = \arcsin\left(\frac{\sigma\lambda}{2\pi}\right).$$

Fig. 9. Plane wave reflectivity versus $\sin\vartheta$ (dashed curves), and angular representation of the normalized Gaussian beam spectra for different beam waists (solid curves, in μm).

The black dashed lines identify the rectangle having the same area of the Gaussian spectrum. This is useful in order to define an equivalent angular spectral width ϑ_{eq} as half of the basis of this rectangle:

$$\vartheta_{\text{eq}} = \arcsin\left(\frac{1}{\sqrt{2\pi}}\frac{\lambda}{2w}\right).$$

The Gaussian beam expansion coefficients are the input data for the plane wave scattering analysis used to obtain the reflected and transmitted fields. Finally, the Gaussian beam reflectivity R_{g} is defined as the ratio of the reflected power to the incident one:

$$R_{\text{g}} = \frac{\iint_{\mathbb{R}^2}\left\|\mathbf{E}^{(\text{refl})}(x,y)\right\|_2^2\,\mathrm{d}x\,\mathrm{d}y}{\iint_{\mathbb{R}^2}\left\|\mathbf{E}^{(\text{inc})}(x,y)\right\|_2^2\,\mathrm{d}x\,\mathrm{d}y}.$$

The plane wave scattering problems are conveniently solved by means of MMT-based schemes. In this work, the grating modes are computed by means of the RCWA, implemented accordingly to the inverse rule formulation, to reduce the TM convergence issue [12].

Each plane wave scattering problem is solved by using $N_{\text{F}} = 31$ Floquet modes in the free-space regions and $N_{\text{G}} = 31$ grating modes in the grating region; according to RCWA, grating modes are represented as a linear combination of N_{h} Floquet modes. To guarantee good accuracy $N_{\text{h}} = 2N_{\text{G}} + 1$ has been used, and a representation of the Gaussian beam which differs of the order of 10^{-3} from the actual beam is obtained with $N_{\text{pw}} = 144$ plane waves.

Figure 7 shows the 0-order TM Floquet mode power reflectivity $R^{(\#9)}$, for different incidence angles. Figure 8 shows the Gaussian beam power reflectivity, $R_{\text{g}}^{(\#9)}$, as a function of the beam waist w.

It appears that narrow beams are poorly reflected; this can be explained by Fig. 9, which shows the normalized Gaussian
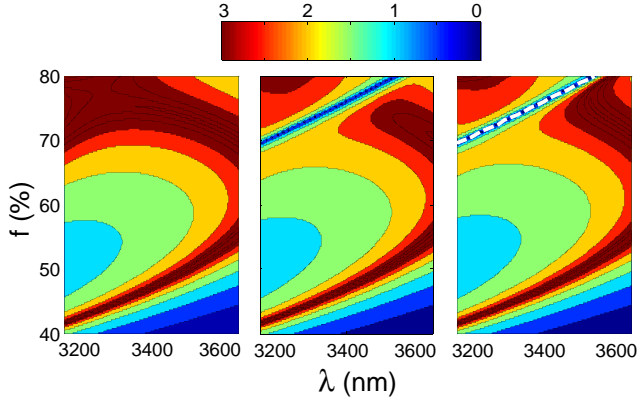
Fig. 10. Number of nines of the power reflectivity maps in the (λ, f) plane. Left: plane wave incidence at $\vartheta = 0°$; center: Gaussian beam reflectivity, $w = 10\,\mu$m; right: off-normal plane wave incidence, $\vartheta = \vartheta_{\text{eq}}$. A narrow reflectivity trench appears for Gaussian and off-normal incidence; the dashed white line estimates its position on the loop-gain analysis basis.

beam spectra for several beam waists (solid curves), and the plane wave reflectivity as a function of the incidence angle ϑ, at λ_1 and λ_2 (dashed curves). The $w = 1\,\mu$m spectrum exhibits significant components in the entire angular range, including the plane wave low reflectivity regions (high ϑ values) at both wavelengths. Instead, in the $w = 10\,\mu$m case, the spectral components are treated very differently at the two wavelengths, causing the difference in the two curves of Fig. 8. Wider beams have narrower spectra, therefore in the remaining cases the spectral components stay within the high reflectivity region. It is worth noting that the normal incident plane wave reflectivity is the asymptotic limit of R_{g} for $w \to \infty$; therefore, R_{g} saturates to the normal incidence value. The reflectivity degradation increases by one order of magnitude the beam waist required to achieve good beam reflection performance (see Fig. 8).

Figure 10 shows a comparison between different ways of computing the TM power reflectivity of the HCG. At left, the usual normal-incidence plane-wave results are provided. In the center, the power reflectivity experienced by a Gaussian beam with $w = 10\,\mu$m is reported. Finally, at right, the plane wave results at $\vartheta = \vartheta_{\text{eq}}$ are given. A reflectivity trench where 100% transmission takes place can be noticed for finite beam size reflectivity. This effect is particularly detrimental in case of tunable VCSELs, because they require a broad-band high reflectivity. Therefore, the normal plane wave incidence is not a wise design framework for small beam size excitation. On the other hand, due to the reasonable agreement of the two results of Fig. 10 (center and right), the ϑ_{eq} incidence plane wave problem can be used as a shortcut to investigate the grating performance. Therefore, since this phenomenon is strongly dependent on both f and λ, the geometry parameters space should be explored so as to avoid the reflectivity trench, considering plane wave reflectivity maps at tilted incidence.

IV. REFLECTIVITY DEGRADATION MECHANISM

To understand the physical mechanism behind the reflectivity degradation phenomenon, the structure has been analyzed
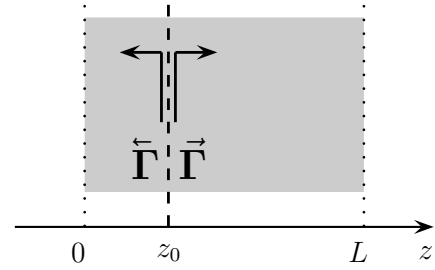

Fig. 11. Sketch of the grating loop gain analysis. The dotted lines identify the grating to free-space interfaces. The reflection coefficients defined in (3) are indicated at $z = z_0$.

as a resonant system. Let $z_0 \in [0, L]$ as in Fig. 11 and let $\overleftarrow{\mathbf{\Gamma}}$ and $\overrightarrow{\mathbf{\Gamma}}$ be the generalized reflection matrices in $z = z_0$; these are computed with the RCWA as the reflection matrices seen from the left and right interfaces and propagated to $z = z_0$ [23]. Then, let $\mathbf{c}^+$, $\mathbf{c}^-$ be the forward and backward power waves in $z = z_0$; therefore,

$$\mathbf{c}^- = \overrightarrow{\mathbf{\Gamma}}\,\mathbf{c}^+ \qquad\qquad \mathbf{c}^+ = \overleftarrow{\mathbf{\Gamma}}\,\mathbf{c}^- \qquad (3)$$

To find a self-consistent solution, the first expression is substituted in the second one, leading to:

$$\overleftarrow{\mathbf{\Gamma}}\,\overrightarrow{\mathbf{\Gamma}}\,\mathbf{c}^+ = \mathbf{c}^+, \qquad (4)$$

where the generalized loop gain matrix $\overleftarrow{\mathbf{\Gamma}}\,\overrightarrow{\mathbf{\Gamma}}$ is full (owing to the modal coupling introduced by the junctions) and is a function of λ, ϑ, and of the grating parameters. Equation (4) suggests that $\mathbf{c}^+$ is the solution of an eigenvalue problem, with eigenvalue t equal to 1; in that case, the power wave reproduces itself after a round trip.

Figure 12 reports $t(\lambda, \vartheta)$, and the corresponding TM reflectivity, for $\vartheta = 3.86°$ (left) and $\vartheta = 0°$ (right). Defining $\lambda_{\text{m}}(\vartheta)$ as the wavelength such that $\angle t(\lambda, \vartheta) = 0$, in Fig. 12 (left) a reflectivity dip lies in its proximity.

Such kind of anomalies in the reflectivity have been reported by Wood at the beginning of 20th Century and are still extensively studied [24]-[33]. Two kinds of anomalies are identified [21]: Rayleigh type (at the wavelengths for which one of the spectral orders emerges from the grating at the grazing angle), and those of resonant type. The latter are related to the excitation of the grating leaky modes, which interfere constructively or destructively with the incident wave, causing sharp reflectivity variations [34]. Since leaky modes are characterized by complex transverse propagation constant ξ and being $\xi^{(\text{inc})} = 2\pi/\lambda \sin\vartheta$ real, it is not possible to observe $|t| = 1$. Indeed, the magnitude of the loop gain eigenvalue is inversely proportional to the imaginary part of ξ.

The $\vartheta = 0°$ case reported in Fig. 12 (left) does not show any reflectivity degradation; this is a very particular situation, since:

- the 0-order Floquet harmonic propagating in the homogeneous space is a real constant function of x;
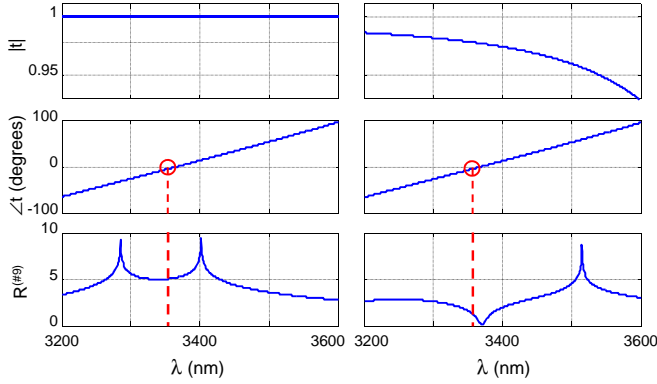- the grating modes are even or odd real functions with respect to x, as shown in Fig. 13 (left).

Fig. 12. The top and center plots show the magnitude and phase of the eigenvalue t versus λ; in these simulations, losses have been neglected. The bottom plots show the TM power reflectivities. The wavelength λ_m coincides with the reflectivity degradation region. At left, $\vartheta = 0°$. At right, $\vartheta = \vartheta_\mathrm{eq}$.
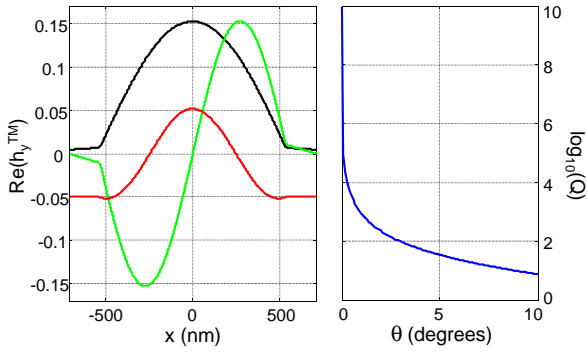

Fig. 13. Left: grating modes (z-propagating) above cutoff at $\lambda = \lambda_\mathrm{m}$, $\vartheta = 0°$. Modes 1, 2, and 3 are drawn in black, light green and red. Right: plot of the Q estimation versus ϑ; $|t|$ is calculated at $\lambda_\mathrm{m}(\vartheta)$, and this is used (5) to estimate the order of magnitude of the quality factor.

Due to these properties, the 0-order Floquet harmonic is orthogonal to the z-propagating odd grating modes; therefore, for $\vartheta = 0°$, this structure supports an x-propagating guided mode. Clearly, the fundamental Floquet harmonic cannot couple with such odd modes, so, no resonance phenomena can affect reflectivity, for $\vartheta = 0°$. By increasing ϑ, the Floquet and grating modes properties change. The lack of symmetry increases progressively the coupling between the formerly orthogonal modes; as a consequence, the reflectivity trench width increases correspondingly. In fact, a lower magnitude of the loop gain eigenvalue leads to a lower Q factor of the resonance [21], whose order of magnitude is related to t [36]:

$$Q(\vartheta) \simeq \left| \frac{1}{1 - t(\lambda_\mathrm{m})} \right|. \tag{5}$$

Figure 13 (right) reports $Q(\vartheta)$ in logarithmic scale; this shows a monotonic increasing behavior, which reaches the upper bound of the working precision at $\vartheta = 0°$ (where $t = 1$, so Q is infinite). This supports the explanation above.

The white dotted line of Fig. 10 identifies $\lambda_\mathrm{m}(f)$; this curve is compatible with the reflectivity trench.

V. CONCLUSION

Unexpected increases of the threshold gain in tunable HCG-VCSELs might occur, depending on the HCG design parameters. This is due to the unrealistic approximation of using a normal-incident plane-wave model as a design framework, which does not account for the beam finiteness. A simplified Gaussian beam excitation model explains the observed phenomena. This is based on a plane-wave representation, where each scattering problem is solved by means of the rigorous coupled wave analysis. The $\vartheta = 0°$ case is a very peculiar condition where no degradation occurs, due to the symmetries of the grating mode functions, as shown in Fig. 13. It is shown that an equivalent plane-wave incidence angle can fairly well reproduce the finite beam reflectivity features (see Fig. 10). This opens up the possibility to perform the HCG design at off-normal incidence, enhancing the design reliability with no additional computation cost.

REFERENCES

[1] R. Michalzik, "VCSELs - Fundamentals, technology and applications of vertical-cavity surface-emitting lasers," *Springer Series in Optical Sciences,* Springer-Verlag, vol. 166, Berlin Heidelberg, 2013.
[2] M. C. Y. Huang, K. B. Cheng, Y. Zhou, A. P. Pisano, and C. J. Chang-Hasnain, "Monolithic integrated piezoelectric MEMS-Tunable VCSEL," *IEEE J. Sel. Topics Quantum Electron.,* vol. 13, no. 2, pp. 374-380, Mar-Apr. 2007.
[3] C. Gierl, T. Gründl, P. Debernardi, K. Zogal, C. Grasse, H. A. Davani, G. Böhm, S. Jatta, F. Küppers, P. Meißner, and M. C. Amann, "Surface micromachined tunable 1.55 μm-VCSEL with 102 nm continuous single-mode tuning," *Optics Express,* vol. 19, no. 18, pp. 17336-17343, Aug. 2011.
[4] C. Gierl, T. Gründl, S. Paul, K. Zogal, M. T. Haidar, P. Meißner, M. C. Amann, and F. Küppers, "Temperature characteristics of surface micromachined MEMS-VCSEL with large tuning range," *Optics Express,* vol. 22, no. 11, pp. 13603-13072, May. 2014.
[5] C. F. R. Mateus, M. C. Y. Huang, Y. Deng, A. R. Neureuther, and C. J. Chang-Hasnain, "Ultrabroadband mirror using low-index cladded subwavelength grating," *IEEE Photon. Technol. Lett.,* vol. 16, no. 2, pp. 518-520, Feb. 2004.
[6] C. J. Chang-Hasnain, Y. Zhou, M. C. Y. Huang, and C. Chase, "High-contrast grating VCSELs," *IEEE J. Sel. Topics Quantum Electron.,* vol. 15, no. 3, May/June 2009.
[7] A. Taghizadeh, G. C. Park, J. Mørk, and I.-S. Chung, "Hybrid grating reflector with high reflectivity and broad bandwidth," *Optics Express,* vol. 22, no. 18, pp. 21175-21184, Sept. 2014.
[8] M. Gebski, M. Dems, A. Szerling, M. Motyka, L. Marona, R. Kruszka, D. Urbańczyk, M. Walczakowski, N. Palka, A. Wójcik-Jedlińska, Q. J. Wang, D. H. Zhang, M. Bugajski, M. Wasiak, and T. Czyszanowski, "Monolithic high-index contrast grating: a material independent high-reflectance VCSEL mirror," *Optics Express,* vol. 23, no. 9, pp. 11674-11686, May 2015.
[9] C. Sciancalepore, B. B. Bakir, S. Menezo, X. Letartre, D. Bordel, and P. Viktorovitch, "III-V-on-Si photonic crystal vertical-cavity surface-emitting laser arrays for wavelength division multiplexing," *IEEE Photon. Technol. Lett.,* vol. 25, no. 12, pp. 1111-1113, June 2013.
[10] M. Fill, P. Debernardi, F. Felder, and H. Zogg, "Lead-chalcogenide mid-infrared vertical external cavity surface emitting lasers with improved threshold: theory and experiment," *Appl. Phys. Lett.,* vol. 103, 201120 (2013).
[11] M. G. Moharam and T. K. Gaylord, "Rigorous coupled-wave analysis of planar-grating diffraction," *J. Opt. Soc. Am.,* vol. 71, no. 7, pp. 811-818, July 1981.

[12] L. Li, "Use of Fourier series in the analysis of discontinuous periodic structures," *J. Opt. Soc. Am. A.,* vol. 13, no. 9, pp. 1870-1876, Sep. 1996.

[13] R. H. Morf, "Exponentially convergent and numerically efficient solution of Maxwell's equations for lamellar gratings," *J. Opt. Soc. Am. A,* vol. 12, no. 5, pp. 1043-1056, May 1995.

[14] A. Tibaldi, R. Orta, O. A. Peverini, G. Addamo, G. Virone, and R. Tascone, "Skew incidence plane-wave scattering from 2-D dielectric periodic structures: analysis by the mortar-element method," *IEEE Trans. Microw. Theory Techn.,* vol. 63, no. 1, pp. 11-19, Jan. 2015.

[15] A. Tibaldi, P. Debernardi, and R. Orta, "Impact of non-ideal shapes on high-contrast grating performance," *Fotonica 2015,* Apr. 2015.

[16] V. Karagodsky, F. G. Sedgwick, and C. J. Chang-Hasnain, "Theoretical analysis of subwavelength high contrast grating reflectors," *Optics Express,* vol. 18, no. 16, pp. 16974-16988, Aug. 2010.

[17] P. Debernardi, R. Orta, and W. Hofmann, "Rigorous, highly-efficient optical tools for HCG-VCSEL design," *SPIE Photonics West*, San Francisco, USA, Feb. 2013.

[18] P. Debernardi and G. P. Bava, "Coupled mode theory: a powerful tool for analyzing complex VCSELs and designing advanced device features," *IEEE J. Sel. Topics Quantum Electron.,* vol. 9, no. 3, pp. 905-917, May/June 2003.

[19] P. Debernardi, R. Orta, T. Gründl, and M. C. Amann, "3-D vectorial optical model for high-contrast grating vertical-cavity surface-emitting lasers," *IEEE J. Quantum Electron.,* vol. 49, no. 2, pp. 137-145, Feb. 2013.

[20] A. Liu, W. Hofmann, and D. H. Bimberg, "Two-dimensional analysis of finite size high-contrast gratings for applications in VCSELs," *J. Opt. Soc. Amer.,* vol. 22, no. 10, May 2014.

[21] A. Hessel and A. A. Oliner, "A new theory of Wood's anomalies on optical gratings," *Applied Optics,* vol. 4, no. 10, Oct. 1965.

[22] P. Debernardi, B. Kögel, K. Zogal, P. Meißner, M. Maute, M. Ortsiefer, G. Böhm, and M.-C. Amann, "Modal properties of long-wavelength tunable MEMS-VCSELs with curved mirrors: comparison of experiment and modeling," *IEEE J. Quantum Electron.,* vol. 44, no. 4, Apr. 2008.

[23] T. Tamir and S. Zhang, "Modal transmission-line theory of multilayered grating structures," *IEEE J. Lightw. Technol.,* vol. 14, no. 5, pp. 914-927, May 1996.

[24] R. W. Wood, "On a remarkable case of uneven distribution of light in a diffraction grating spectrum," *Proc. Phys. Soc. London,* vol. 18, pp. 269-275, 1902.

[25] Lord Rayleigh, "On the dynamical theory of gratings," *Proc. R. Soc. Lond.,* vol. 79, pp. 399-416, 1907.

[26] S. S. Wang, R. Magnusson, J. S. Bagby, and M. G. Moharam, "Guided-mode resonances in planar dielectric-layer diffraction gratings," *J. Opt. Soc. Am. A,* vol. 7, no. 8, Aug. 1990.

[27] S. Peng and M. Morris, "Resonant scattering from two-dimensional gratings," *J. Opt. Soc. Am. A,* vol. 13, no. 5, May. 1996.

[28] R. Magnusson and M. Shokooh-Saremi, "Physical basis for wideband resonant reflectors," *Optics Express,* vol. 16, no. 5, pp. 3456-3462, Feb. 2008.

[29] Y. Zhou, M. Moewe, J. Kern, M. C. Y. Huang, and C. J. Chang-Hasnain, "Surface-normal emission of a high-Q resonator using a subwavelength high-contrast grating," *Optics Express,* vol. 16, no. 22, pp. 17282-17287, Oct. 2008.

[30] K. X. Wang, X. Yu, S. Sandhu, and S. Fan, "Fundamental bounds on decay rates in asymmetric single-mode optical resonators," *Optics Letters,* vol. 38, no. 2, Jan. 2013.

[31] Z. Wang, B. Zhang, and H. Deng, "Dispersion engineering for vertical microcavities using subwavelength gratings," *Phys. Rev. Lett.,* prl. 114, 073601, 2015.

[32] A. Taghizadeh, J. Mørk, and I.-S. Chung, "Vertical-cavity in-plane heterostructures: physics and applications," *arXiv preprint [physics.optics],* arXiv:1508.01044, Aug. 2015.

[33] A. Liu, W. Hofmann, and D. H. Bimberg, "Integrated high-contrast-grating optical sensor using guided mode," *IEEE J. Quantum Electron.,* vol. 51, no. 1, Jan. 2015.

[34] H. L. Bertoni, L.-H. S. Cheo, and T. Tamir, "Frequency-selective reflection and transmission by a periodic dielectric layer," *IEEE Trans. Antennas Propag.,* vol. 37, no. 1, pp. 78-83, Jan. 1989.

[35] N. Gregersen, S. Reitzenstein, C. Kistner, M. Strauss, C. Schneider, S. Höfling, L. Worschech, A. Forchel, T. R. Nielsen, J. Mørk, and J.-M. Gérard, "Numerical and experimental study of the Q factor of high-Q micropillar cavities," *IEEE J. Quantum Electron.,* vol. 46, no. 10, Oct. 2010.

[36] N. Gregersen, S. Reitzenstein, C. Kistner, M. Strauss, C. Schneider, S. Höfling, L. Worschech, A. Forchel, T. R. Nielsen, J. Mørk, and J.-M. Gérard, "Numerical and experimental study of the Q factor of high-Q micropillar cavities," *IEEE J. Quantum Electron.,* vol. 46, no. 10, pp. 1470-1483, Oct. 2010.

Alberto Tibaldi was born in Casale Monferrato, Italy, on February 21, 1987. In July 2009, November 2011 and January 2015 he received the B.Sc., M.Sc. (*summa cum laude*) and Ph.D. degrees in Electronic Engineering from the Politecnico di Torino. In 2012 he joins the Applied Electromagnetics and Electronic Devices Group of the Istituto di Elettronica e di Ingegneria dell'Informazione e delle Telecomunicazioni (IEIIT) of the Consiglio Nazionale delle Ricerche (CNR) as research fellow. In 2013 he was a visiting member of the Terahertz Sensing Group, Delft University of Technology, Delft, The Netherlands. His scientific interests include the numerical simulation of electromagnetic passive devices.

Pierluigi Debernardi received his degree in Electronics Engineering in 1987 from Politecnico di Torino, Torino, Italy. Since 1989 he's with the Italian National Council of Research at Politecnico di Torino. His interests are mainly in the field of the modeling of semiconductor materials and devices for optoelectronic applications. Recently he is mostly involved in modeling and designing VCSEL structures with non-circular and/or complex geometries, so as to achieve specific performances.

Renato Orta is a member of the Department of Electronics, Politecnico di Torino, since 1974. He joined the Department as Assistant Professor, in 1987 became Associate Professor and since 1999 is Full Professor. He currently teaches courses on electromagnetic field theory and optical components. His research interests include the areas of microwave and optical components, radiation and scattering of waves and numerical techniques. He is Senior Member of the IEEE.